Draft version October 18, 2016
Preprint typeset using LaTeX style emulateapj v. 5/2/11

arXiv:1610.04862v1 [astro-ph.CO] 16 Oct 2016

THE EFFECT OF CORNER MODES IN THE INITIAL CONDITIONS OF COSMOLOGICAL SIMULATIONS

B. Falck[1], N. McCullagh[2], M. C. Neyrinck[2,3,4], J. Wang[5], A. S. Szalay[3]

Draft version October 18, 2016

ABSTRACT

In view of future high precision large scale structure surveys, it is important to quantify percent and sub-percent level effects in cosmological N-body simulations from which theoretical predictions are drawn. One such effect involves the choice of whether to set all modes above the one-dimensional Nyquist frequency, the so-called "corner" modes, to zero in the initial conditions. By comparing simulations with and without these modes, we find that at $z > 6$, the difference in the matter power spectrum is large at wavenumbers just below $k_{\rm Ny}$, reducing to below 2% at all scales by $z \sim 3$. Including corner modes results in a better match between a low-resolution simulation and a high-resolution simulation at wavenumbers around the Nyquist frequency of the low-resolution simulation. The differences in mass functions are 3% for the smallest halos at $z = 6$ for the simulation resolution studied here ($m_p \sim 10^{11}\, h^{-1}\, M_\odot$), but we find no significant difference in the stacked profiles of well-resolved halos at $z \leq 6$. Thus removing power at $k > k_{\rm Ny}$ in the initial conditions of cosmological simulations has a small effect on small scales and high redshifts, typically below a few percent, and may be important to take into account in simulations of the high redshift universe.

Subject headings: dark matter – large-scale structure of Universe – methods: numerical

1. INTRODUCTION

The growth of structure in the Universe is a highly nonlinear process, making it difficult to calculate precise theoretical predictions for the late-time distribution of large scale structure. Cosmological N-body simulations have revolutionized our understanding of large scale structure in the Universe by numerically solving for the nonlinear gravitational collapse of matter, enabling us both to test and rule out cosmological theories and to calibrate analysis methods used on observations (for reviews, see Efstathiou et al. 1985; Bertschinger 1998). As computer hardware and numerical algorithms have improved over the decades, cosmological simulations have been able to simulate larger volumes and higher resolutions and include non-standard cosmological models and complex baryonic physical processes, increasing the accuracy with which we can model the formation of structure in the Universe.

As future cosmological surveys push their measurements to higher and higher precision (e.g. Euclid, WFIRST, DESI, LSST, and SKA), it is important that theoretical predictions taken from numerical simulations do not significantly contribute to the error in the derived cosmological parameters. This means both that the numerical codes must be pushed to higher accuracy and that previously minor processes must be taken into account. Authors of numerical codes perform their own consistency checks on problems with known analytical solutions, nevertheless small but measurable differences remain in full cosmological N-body simulations (Heitmann et al. 2008, 2010; Schneider et al. 2015). Even if different numerical codes agreed, pushing simulations to higher accuracy requires taking into account effects such as, for example, how the initial conditions are generated (Crocce et al. 2006; L'Huillier et al. 2014), the choice of starting redshift (Heitmann et al. 2010; Reed et al. 2013; McCullagh et al. 2016), the force softening (Smith et al. 2014), general relativistic effects (Christopherson et al. 2015; Thomas et al. 2015), and baryonic effects (van Daalen et al. 2011).

We focus here on the generation of initial conditions. Many methods and publicly available codes exist (e.g. Bertschinger 1995; Pen 1997; Bertschinger 2001; Sirko 2005; Crocce et al. 2006; Jenkins 2010; Hahn & Abel 2011; Jenkins 2013), some of which are designed to work with a specific N-body code. Generating initial conditions involves first calculating the spectrum of density perturbations at some high redshift given a background cosmological model. If the primordial density fluctuations are Gaussian, which occurs in the simplest models of inflation, then their statistics are fully specified by the power spectrum, $P(k)$. The cosmic variance from realization to realization consists of different sets of Fourier phases, and amplitudes consistent with $P(k)$. The power spectrum can be written as the product of a power law spectrum (with power given by n_s, the spectral index after inflation) with random phases and the transfer function that represents the linear evolution of each mode. The transfer function can be calculated numerically (e.g. LINGER (Ma & Bertschinger 1995), CMBFast (Seljak & Zaldarriaga 1996), CAMB (Lewis et al. 2000), or CLASS (Blas et al. 2011)) or using approximate analytical expressions (e.g. Eisenstein & Hu 1998). This random phase realization of a given power spectrum must then be discretized to a grid of some resolution, depending on the requirements of the simulation. Dark matter particle positions and velocities at

[1] Institute of Theoretical Astrophysics, University of Oslo, PO Box 1029 Blindern, N-0315, Oslo, Norway
[2] Institute for Computational Cosmology, Department of Physics, Durham University, Durham DH1 3LE, UK
[3] Department of Physics and Astronomy, Johns Hopkins University, 3400 N Charles St, Baltimore, MD 21218, USA
[4] Institut d'Astrophysique de Paris, 98 bis boulevard Arago, 75014, Paris, France
[5] National Astronomy Observatories, Chinese Academy of Science, Datun Road, Beijing, PR China

a (chosen) high redshift are obtained by perturbing the discretized initial power spectrum from either a uniform grid or a force-neutral "glass" configuration, according to first order (the Zel'dovich approximation, Zel'dovich 1970) or second order Lagrangian perturbation theory (2LPT).

Each step in the generation of initial conditions involves choices which affect the numerical accuracy of the high redshift density field or power spectrum and which can propagate to lower redshift. For example, the real space density field can either be calculated by inverse transforming the Fourier space transfer function or by convolving the white noise field with the real space transfer function, and this choice affects whether the power spectrum or the correlation function is modeled more accurately in a finite box (Pen 1997; Sirko 2005; Hahn & Abel 2011). Another choice is between grid and glass initial conditions: particle positions at low redshift retain their grid-like structure in voids when initialized on a uniform grid, which some may think has aesthetic drawbacks; on the other hand, the density field from glass initial configurations contains spurious clustering on small scales at high redshift, though this does not grow (L'Huillier et al. 2014). In this paper we investigate the effect of a particular choice – whether power for $|\mathbf{k}|$ modes greater than the one-dimensional Nyquist frequency, which we call "corner modes," are retained or zeroed.

A Gaussian random field sampled on a lattice can be written as the convolution of white noise with the transfer function (Efstathiou et al. 1985; Salmon 1996; Bertschinger 2001):

$$\delta\left(\mathbf{x}\right) = \left(\xi \star T\right)\left(\mathbf{x}\right) = \int d^3x' \, \xi\left(\mathbf{x}'\right) T\left(\left|\mathbf{x} - \mathbf{x}'\right|\right), \quad (1)$$

where $\xi(\mathbf{x})$ is Gaussian white noise. Setting up initial conditions is thus a problem of representing a random phase realization of a given power spectrum by a discrete set of particles in a simulation volume. This can be carried out by computing the transfer function and white noise field in Fourier space, followed by an inverse Fourier transform, or by convolving an inverse transform of $T(k)$ with the white noise field as in Equation 1. Though $P(k)$ is isotropic, because of the Cartesian discretization of k-space, the initial conditions are set for $0 < (k_x, k_y, k_z) < k_{\mathrm{Ny}}$, where $k_{\mathrm{Ny}} = \pi N/L$ is the Nyquist frequency, N is the cube root of the total number of particles, and L is the length of the cubic box. This means that there is non-zero power at modes whose modulus is larger than the Nyquist frequency, $|\mathbf{k}| > k_{\mathrm{Ny}}$, in the corners of the k-space cube, i.e., corner modes.

One can choose to remove corner modes in the initial conditions by applying some additional filtering, such as the spherical Hanning filter used by Bertschinger (2001), or by explicitly zeroing the power for $|\mathbf{k}| > k_{\mathrm{Ny}}$. Note that if transfer function is sampled in real space, the choice of whether to remove corner modes is not explicit, but e.g. the finite-difference approach of Hahn & Abel (2011) has similar filtering properties to the Hanning filter, with a relatively sharp cut-off in k-space. This results in the damping of small scale power (below k_{Ny}) which can be corrected, though these corrections will lead to spectral leakage and associated spurious oscillations (Hahn & Abel 2011). Corner modes are often removed in initial conditions generators, but not always, and there is not always a mention of the choice. For example, they are kept in an early version of GRAFIC in order to retain all power present in the initial density field (Bertschinger 1995) but removed in GRAFIC2 with a note that the effect of the 'anisotropy' needs to be studied (Bertschinger 2001). So far, the effects of the choice whether to keep or zero corner modes have not been studied in detail, which we aim to do in this paper.

One argument for removing corner modes is that it enforces isotropy and spherical symmetry in Fourier space, but we argue here that this is not the case for a discretely sampled density field in a periodic box.

First suppose we have a continuous sinusoidal signal $f(x) = \sin(k_0 x)$ in one dimension which is sampled at regular intervals a. The discrete sampled signal $g(x)$ can be written as

$$g(x) = f(x) \sum_m \delta(x - ma). \quad (2)$$

It turns out that there are infinite frequencies that give exactly the same set of samples. With $k_s = 2\pi/a$, the signal $f_n(x) = \sin((k_0 + nk_s)x)$ sampled the same way gives

$$g_n(x) = f_n(x) \sum_m \delta(x - ma) = \sin((k_0 + nk_s)ma) = g(x). \quad (3)$$

This shows that the frequency spectrum contains an infinite series of replicas of the original frequency spectrum shifted by k_s, a property known as spectral replication. This periodic replication of the spectrum is entirely due to the discrete sampling.

Now consider a density field sampled on a cubic grid with Nyquist frequency k_{Ny}. For simplicity, let us use an uncorrelated (white noise) random process to populate the density in a box of size N^3. The Fourier transform of this field will have independent modes with N^3 degrees of freedom, i.e. the corners are filled. As we sample this cubic volume at a regular rate along all three axes, the Fourier space is replicated in a way similar to how periodic boundary conditions behave in configuration space. This spectral replication is a consequence of the axis-parallel, regular sampling.

This 3-dimensional spectral replication is illustrated in Figure 1. We show the replicated envelope of the power spectrum in the cases when the corner modes are removed (left) and the corner modes are left intact (right). It is apparent that the replicated pattern is not isotropic when the corner modes are removed, while the Fourier modes fill the available space uniformly when the corner modes are kept. Though the pattern of mirror frequencies occurs on scales smaller than initially resolved, these modes will become relevant at lower redshifts as structure forms on scales smaller than the inter-particle separation; indeed, as we will show, even if corner modes are removed in the initial conditions, modes at $|\mathbf{k}| > k_{\mathrm{Ny}}$ emerge naturally through non-linear mode-mode coupling and grow as the simulation evolves. Note also that the corner and non-corner modes are entirely independent; there is no aliasing of modes above the Nyquist frequency to lower frequencies since spectral replication only occurs parallel to each axis.

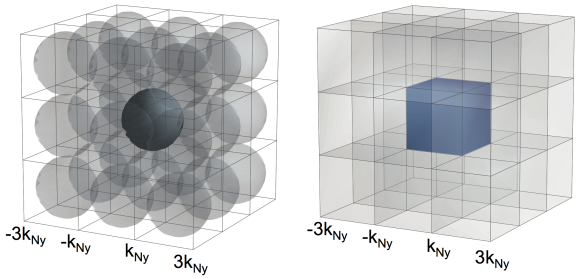

Figure 1. We illustrate the effect of the corner mode removal through displaying the envelope of the power for a flat, white noise power spectrum. The grids shown are in Fourier space, and the grids outside the central grid show the power that is mirrored to higher frequencies. From the figure on the left, one can see that the power spectrum after the removal of the corner modes is anisotropic, whereas the figure on the right shows that preserving the corner modes also preserves isotropy.

In Figure 2 we visually show the difference that corner modes make in the initial conditions for a realization of a Gaussian random field, generated with the same initial power spectrum as used below, linearly extrapolated to $z = 0$. Here, we show a 2D, 32^2 slice of a 32^3 grid of pixels spaced by $\frac{1000}{512}\,h^{-1}\,\mathrm{Mpc}$ (the same spacing as in the 512^3 particle simulation used below). Zeroing the corner modes visibly smooths the density field, and the difference field, essentially a Gaussian field with only corner modes, has visible fluctuations as well.

In this paper we determine the effect of including vs. removing corner modes in the initial conditions of cosmological simulations. In Section 2, we describe the set of simulations used for this test, and in Section 3 we measure the effect of these corner modes on the matter power spectra, one point density distribution functions, halo mass functions, and halo density profiles at several redshifts. Conclusions and discussion are presented in Section 4.

2. SIMULATIONS

To determine the effect of including or removing corner modes in the initial conditions of simulations, we run two full cosmological dark matter N-body simulations where the only difference is whether these modes are present. The simulations were run using the L-Gadget2 code (Springel 2005) with a box length of $1\,h^{-1}\,\mathrm{Gpc}$, 1024^3 particles, and WMAP7 cosmological parameters ($\Omega_M = 0.272$, $\Omega_\Lambda = 0.728$, $h = 0.704$, $\sigma_8 = 0.81$, $n_s = 0.967$) (Komatsu et al. 2011). Each dark matter particle has a mass of $m_p = 7.031 \times 10^{10}\,h^{-1}\,M_\odot$, and the Nyquist frequency of the simulation is $k_{\rm Ny}= \pi N/L = 3.2\,h\,\mathrm{Mpc}^{-1}$. Initial conditions are generated using IC_2lpt_Gen (Jenkins 2013), and both simulations have the same random phases. The starting redshift is $z = 127$ and was generated using 2^{nd} order Lagrangian perturbation theory, sampled on a grid; 64 snapshots are saved down to $z = 0$. These simulations were run as part of Indra, a suite of 512 simulations with the same box size, particle number, and cosmological parameters with the goal of beating down cosmic variance in large scale structure studies (Falck, et al., *in preparation*). This means that the box size and resolution are chosen to give good statistics on large scales instead of resolving very small scales.

Even if a difference is found between the simulation where these corner modes are present in the initial conditions and where they are zeroed, it would be unclear which is 'correct'. To address this, we also run downgraded versions of both simulations (with and without corner modes) with 512^3 particles and the same box size of $1\,h^{-1}\,\mathrm{Gpc}$. Then we can compare the downgraded resolution simulation to the higher resolution simulation and determine whether the presence of corner modes has an effect on how well, and at what scales, the lower resolution simulation converges to the 'truer' higher resolution simulation. For these, the mass of each dark matter particle is $5.62\times10^{11}\,h^{-1}\,M_\odot$, and the Nyquist frequency is $k_{\rm Ny}= 1.61\,h\,\mathrm{Mpc}^{-1}$.

Halo catalogs are generated as the simulation runs using a standard friends-of-friends algorithm (FOF; Davis et al. 1985), with a linking length of $b = 0.2$ times the inter-particle separation, L/N, and a minimum of 20 particles per halo. Post-processing of the FOF halos is performed with SUBFIND (Springel et al. 2001) to identify subhalos in phase space. Centers are calculated for the main FOF halo and any subhalos as the minimum of the potential well, defined by the position of the most bound particle; we use these centers in the following section to measure density profiles of the FOF halos.

3. RESULTS

First, in Figure 3, we visually show the difference in $z = 0$ particle positions between the simulations with and without corner modes, from the degraded-resolution 512^3-particle simulations. The differences are small in voids and larger in high-density regions. At high density, not only is non-linearity inherently stronger, but there are more close encounters among particles, giving increased opportunity for numerical noise. Thus, it is not surprising that small initial differences get most amplified in the final conditions at high densities.

In this 512^3-particle simulation, the distribution of displacements between $z = 0$ positions in the simulations with and without corner modes has a median of 0.34 and a root mean square (rms) of $0.61\,h^{-1}\,\mathrm{Mpc}$. If the displacement between positions with and without corner modes were Gaussian in each dimension, the distribution of squared distances would be a χ^2 with 3 degrees of freedom. Assuming this distribution, an rms distance of $0.61\,h^{-1}\,\mathrm{Mpc}$ would give a median distance of $\sim 0.55\,h^{-1}\,\mathrm{Mpc}$, much larger than the measurement. This non-Gaussianity in the displacements in each dimension accords with the visual impression of Figure 3 that most displacements are tiny (in low-density areas), with a heavy larger-displacement tail (in high-density regions).

3.1. *Power Spectra*

In this section, we consider the differences in the power spectra between the simulations with and without corner modes over a range of redshifts. Power spectra were measured using the POWMES code (Colombi et al. 2009), which interpolates the particles to a grid and computes the spectrum using Fast Fourier Transform (FFT). We

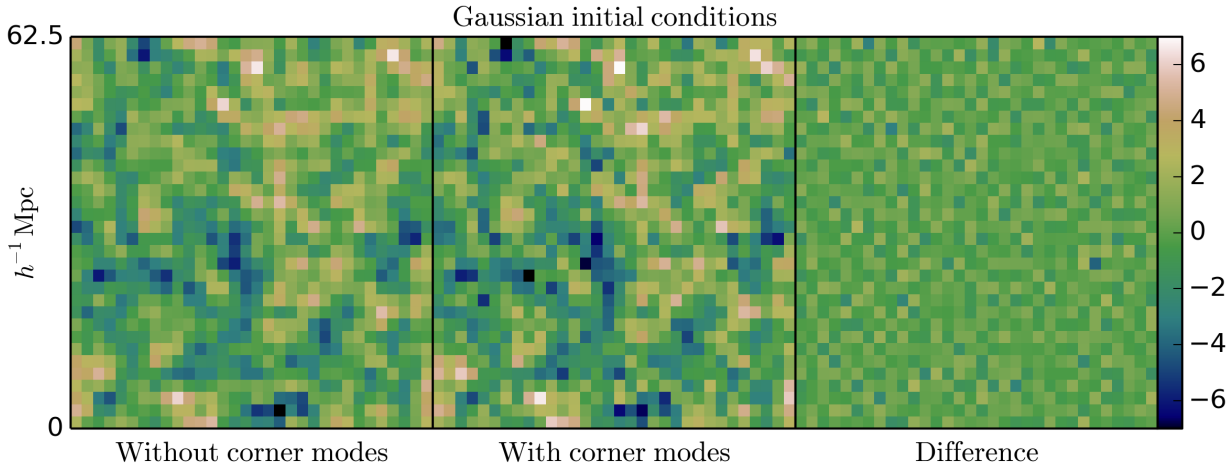

Figure 2. Visual differences between initial-conditions density fields with and without corner modes. The density fields were extrapolated in Eulerian linear theory to $z = 0$, and the panels are square, $62.5\,h^{-1}$ Mpc on a side. These density fields have essentially the properties of the initial conditions of the 512^3 simulation below, although the realization is different.

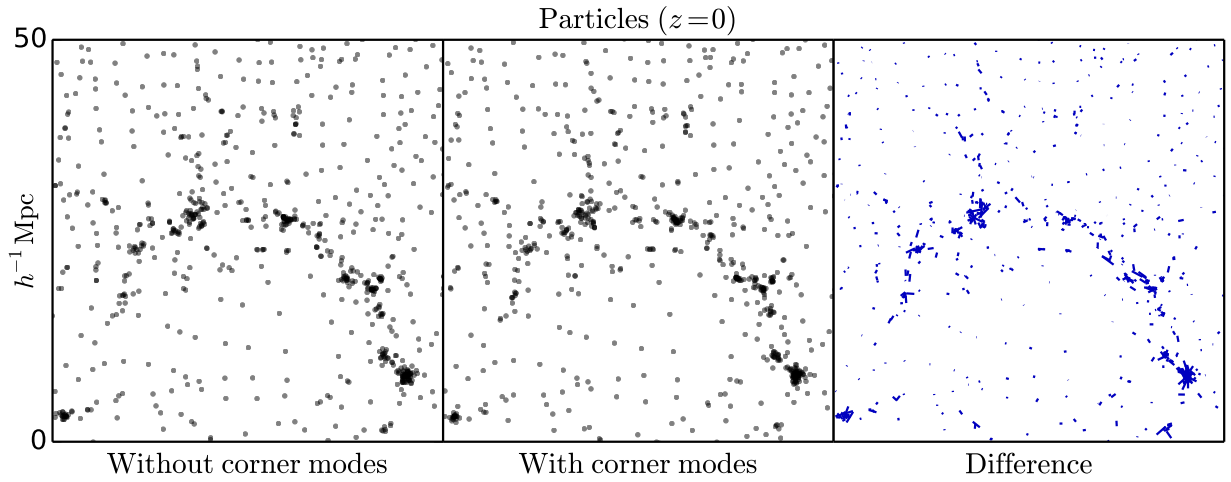

Figure 3. Visual differences between $z = 0$ particle positions with and without corner modes. The square panels, $50\,h^{-1}$ Mpc on a side, show particles on the same 2D initial-conditions sheet, taken from the degraded-resolution simulations described in the text, with initial inter-particle spacing $\sim 2\,h^{-1}$ Mpc. At right, small lines are drawn between positions of particles with and without corner modes.

used a cloud-in-cell (CIC) density assignment scheme on a 1024^3 grid. POWMES computes the raw power spectrum, as well as the spectrum corrected for the CIC window function and aliasing effects. To study the corner modes in detail, we slightly modified the binning scheme in POWMES to ensure that the particle Nyquist frequency is at the edge of a bin, so that there is no mixing of the corner modes into the bin below the Nyquist frequency.

Figure 4 shows power spectra at several redshifts for both high resolution (1024^3 particles) simulations along with the initial linear theory power spectrum, computed using CAMB (Lewis et al. 2000). There is good agreement with the linear theory power spectrum for both simulations at the starting redshift, $z = 127$; near the Nyquist frequency (of both the particle distribution and the CIC density grid, $k_{\rm Ny} = 3.2\,h\,{\rm Mpc}^{-1}$), the power spectrum is enhanced above the theoretical power spectrum as expected for a moderately perturbed grid of particles such as is the case for very early snapshots (Marcos et al. 2006; Joyce & Marcos 2007; Colombi et al. 2009; Garrison et al. 2016). The simulations with and without corner modes agree very well up to the Nyquist frequency at all redshifts; for k at and just above $k_{\rm Ny}$, at high redshift the power spectrum abruptly cuts off in the simulation where these modes are zeroed. The dramatic upturn in the high-redshift power spectra at wave numbers above $k_{\rm Ny}$ is due to the window function correction and is not observed in the raw power spectra. Modes just above $k_{\rm Ny}$ in the simulation with corner modes removed are slowly restored as $z \to 0$ via non-linear mode-mode coupling, until both power spectra agree well at all k at around $z = 3$.

Figure 5 shows the ratio of power spectra in simulations without corner modes to those where they are included, for the same redshifts as Figure 4. At high-z the ratio is close to 1 up to the Nyquist frequency, where it diverges, as expected. As $z \to 0$ the ratio flattens out, creating differences both above and below $k_{\rm Ny}$, such that the simulation with no corner modes in the initial conditions has less power than the simulation with corner modes at frequencies above about 2.5 $h\,{\rm Mpc}^{-1}$. The deviations in the power spectra below the Nyquist frequency arise

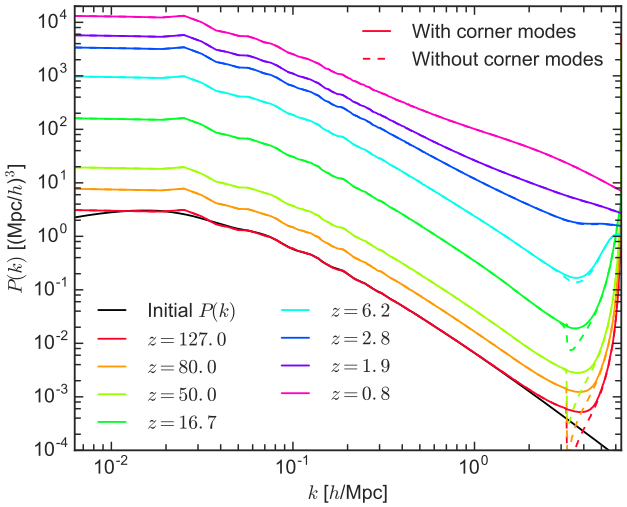

Figure 4. Measured power spectra at a range of redshifts covering the evolution of the simulation along with the theoretical input power spectrum. Solid lines show simulations including corner modes and dashed lines show simulations with these modes zeroed.

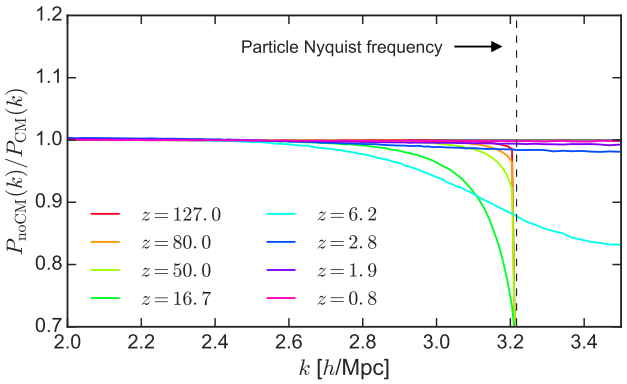

Figure 5. Ratio of PS without corner modes to with corner modes at a few redshifts, focusing on the high-k deviation. The vertical dashed line shows the Nyquist frequency, beyond which there is no power in the simulations without corner modes. As redshift decreases, the ratio approaches 1 at all scales.

from the coupling between the corner modes and lower frequency modes as the simulations progress. By the lowest redshift shown, $z = 0.8$, the power spectra from the two simulations very nearly agree, the differences present at high redshift having become fully washed out by nonlinear evolution.

We examine these differences in greater detail in Figure 6, which is the same as Figure 5 but zoomed in to show small percentage deviations at $k > 1\ h\,\mathrm{Mpc}^{-1}$. Interestingly, at intermediate redshifts, there is an increase in power in the simulation with no corner modes relative to the simulation with corner modes for frequencies $k < 2.5\ h\,\mathrm{Mpc}^{-1}$. The maximum deviation is $\sim 0.4\%$ at $k \sim 2\,h\,\mathrm{Mpc}^{-1}$ at $z = 2.8$. The deviation decreases below $z = 2.8$, and the ratio is again close to 1 for $z = 0.8$.

In order to determine whether including corner modes is "better" than zeroing them out in the initial conditions, we compare the low-resolution simulations with and without corner modes to their high-resolution counterparts. Figure 7 shows the ratio of the simulations with 512^3 particles to the corresponding high-resolution simulation. The top panel shows the ratio for the simulations with corner modes and the bottom panel shows the ratio for simulations without corner modes. For the earliest snapshots, both ratios are enhanced above unity near the Nyquist frequency of the particles in the lower resolution simulation (given by the vertical dashed line at $k = 1.6\ h\,\mathrm{Mpc}^{-1}$). This is because the particles are on a very nearly uniform grid, as we discussed for the high-redshift power spectra in Figure 4. In the simulations without corner modes, at high redshift the ratio drops sharply at the Nyquist frequency of the lower resolution simulation, while the ratio of the simulations with corner modes has no such discontinuity. As redshift decreases, this absence of power in the simulation without corner modes leaks to scales below Nyquist, and both ratios flatten out, though the ratio including corner modes is closer to 1. At all redshifts, the ratio for the simulations with corner modes is smoother across the Nyquist boundary.

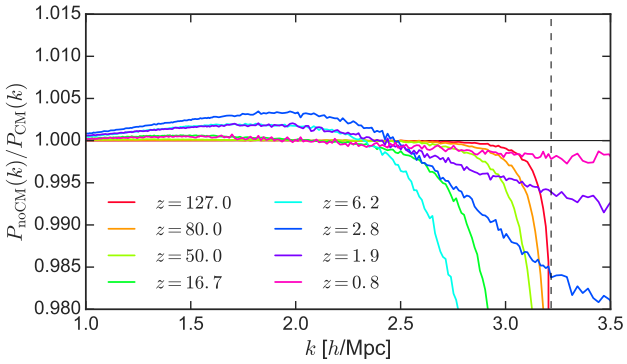

Figure 6. The same as Figure 5, but focusing on the small percentage deviations at $k > 1\,h\,\mathrm{Mpc}^{-1}$.

These results suggest that including corner modes in the lower resolution simulation results in a power spectrum that is closer to the higher-resolution counterpart. However, these effects are much smaller than resolution effects, which cause the power spectra in both cases to differ from the high resolution case by as much as 20%, even after the particles are sufficiently displaced from the grid. Also, the resolution affects a much wider range of wavenumbers ($0.6 < k < k_{\rm Ny}\,h\,\mathrm{Mpc}^{-1}$) than the corner modes, which only affect the power spectra very close to the Nyquist frequency.

3.2. *1-point PDFs of Density*

In this section we explore the effect of the corner modes on the 1-point probability distribution functions (PDFs) of the overdensity at various redshifts. The PDF is the lowest-order statistic of the matter-density field. It is sensitive to phase correlations and therefore visual differences in the density field (Neyrinck 2014). The PDF can be difficult to model, but recently, spherical dynamics have been shown to be remarkably accurate to model it, both for a mass-weighted PDF (Neyrinck 2013) and a volume-weighted PDF (Bernardeau et al. 2014; Uhlemann et al. 2016). A matter-density PDF, if it can be inferred observationally, would provide impressive cosmological constraints (Codis et al. 2016).

We compute the overdensity field using a CIC assign-

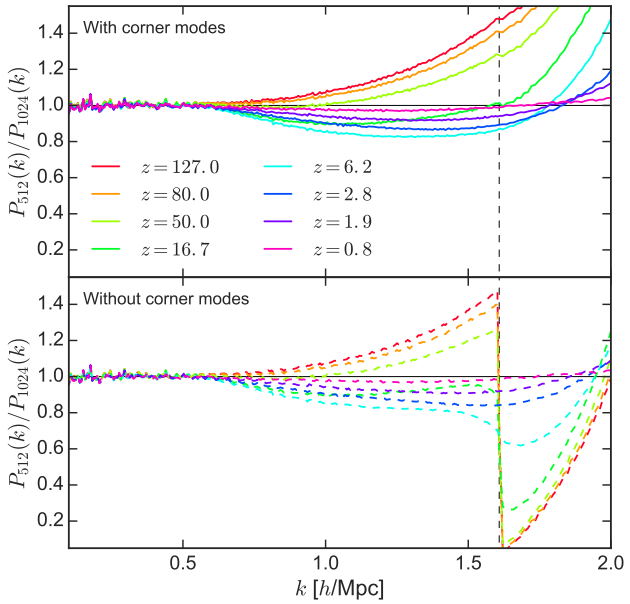

Figure 7. Ratio of PS of low resolution simulation to PS of high resolution simulation, for simulations with (solid, upper panel) and without (dashed, lower panel) corner modes.

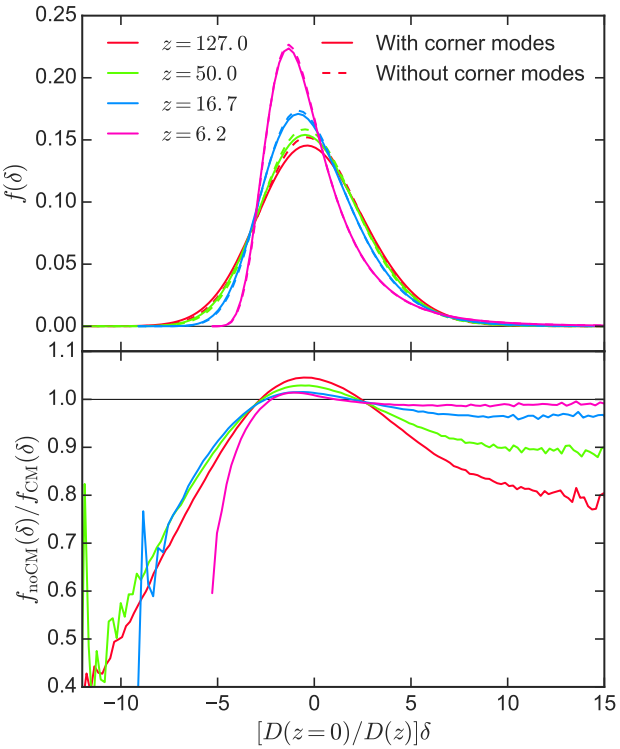

Figure 8. Top: one point distribution functions of the overdensity field using CIC density assignment in 1 h^{-1} Mpc cells from simulations with and without corner modes, at several redshifts. Bottom: Ratio of distribution functions without corner modes to those with corner modes.

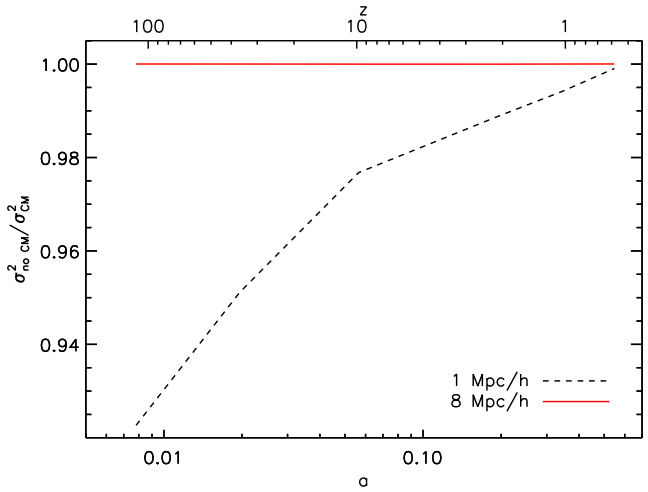

Figure 9. Ratio of the variance of the one point PDF without corner modes to that with corner modes as a function of redshift, using both $1\,h^{-1}$ Mpc cells (dashed) and $8\,h^{-1}$ Mpc cells (solid).

ment scheme with $\frac{1000}{1024} \approx 1\,h^{-1}$ Mpc cells. The overdensity PDFs are plotted in Figure 8 at several redshifts. To aid comparison, we scale δ with the inverse growth factor $[D(z=0)/D(z)]$, allowing us to compare just the shapes of the distributions. We only show PDFs for $z > 6.2$ because at lower redshift the differences are negligible.

The bottom panel of Figure 8 shows the ratio of the PDFs in the simulation without corner modes to that with corner modes. The PDFs without corner modes are narrower, thus the ratio is suppressed at low and high densities and enhanced near $\delta = 0$. There is a strong redshift dependence at high densities: removing corner modes suppresses high densities by 20% at the initial redshift, reducing to $\sim 5\%$ at $z = 16.7$ and $\sim 1\%$ at $z = 6.2$ as these modes become repopulated during the evolution of the simulation.

To quantify the evolution of the difference in the density distribution functions with redshift, we measure the variance of the PDFs using both $1\,h^{-1}$ Mpc and $8\,h^{-1}$ Mpc CIC grid cells at several redshifts. The ratios of these variances in the no corner mode simulation to those with corner modes are shown in Figure 9. Zeroing the corner modes reduces the $1\,h^{-1}$ Mpc variance in the density field at high redshift compared to leaving them, and this difference reduces to $\sim 0.05\%$ at $z = 1$, while the difference in the $8\,h^{-1}$ Mpc variance is negligible.

Note that this variance ratio depends on the logarithmic slope of the initial power spectrum at $k_{\rm Ny}$ and therefore also on the simulation resolution. If the slope is steep (at high resolution, for a typical ΛCDM simulation), the fractional power removed at the initial interparticle scale by zeroing corner modes will be less than for a shallower slope. Assuming the same ΛCDM linear power spectrum as used in these simulations, changing the simulation resolution by a factor of 10 changes the effect of corner modes on the variance of the overdensity PDF by a few percent.

3.3. *Halo Mass Functions*

In Figure 10 we plot halo total mass functions at 10 redshifts from $z = 6.2$ to $z = 0$. Note that these are not mass functions for virial masses or M_{200}, since we did not want our results to depend on additional post-processing of the halos. There are tiny differences in the cumulative mass functions of the simulations with and without corner modes in the initial conditions, mostly at the high mass end. Though these differences occur at all

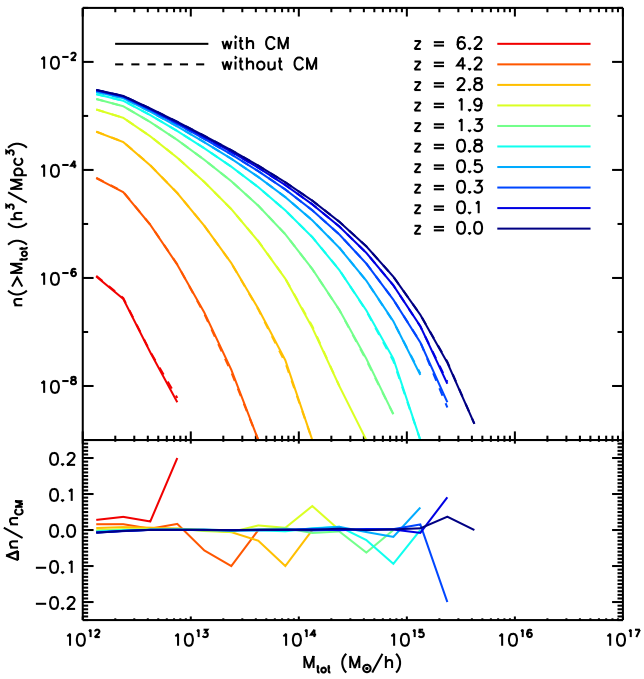

Figure 10. Top panel: total mass functions of FOF halos from $z = 6.2$ to $z = 0$ for the simulation with (solid) and without (dashed) corner modes. Bottom panel: ratio of mass functions without to with corner modes.

redshifts, they are not systematic – sometimes mass functions from the simulation with corner modes are higher than those without corner modes, sometimes lower – and the differences are very small. This can be seen in the bottom panel of Figure 10, which shows the ratio of the mass functions from the simulation without corner modes to the simulation with corner modes. The largest differences, up to 20% but mostly within 10%, are in the largest mass bins at a given redshift.

There is also a small difference in the number of small halos, with total masses less than $3 \times 10^{12}\, h^{-1}\, M_\odot$. Note that the smallest halos, containing 20 particles, have masses of $1.3 \times 10^{12}\, h^{-1}\, M_\odot$. At $z = 6.2$, there are 3% more small halos in the simulation without corner modes; this difference reduces as $z \to 0$ and is less than 1% by $z = 2.8$. Interestingly, the ratio dips slightly below zero at $z = 2$ and continues to decrease, such that by $z = 0$ there are 0.7% fewer small halos in the simulation without corner modes than with corner modes. Recall that the ratio of power spectra without corner modes to those with corner modes is also increased between $k = 1$ and $k = 2.5\, h\,\mathrm{Mpc}^{-1}$ until $z \sim 2$ (see Figure 6), so this seems to be also reflected in the low end of the mass functions. Though these differences at the low end of the mass function are for halos with fewer than 50 particles, note that higher resolution simulations will resolve halos at even higher redshifts, where the effect of removing corner modes is larger. It will be important to take this effect into account in high resolution simulations of the high redshift universe.

To determine whether the presence of corner modes has an effect on how well a simulation converges to a higher resolution simulation, we compare the mass functions with and without corner modes to the downgraded resolution simulations in Figure 11. We show mass functions with 1024^3 and 512^3 particles (starting from the minimum mass of the lower resolution simulations for both) in the top panels, and the bottom panels show the ratios of the lower to higher resolution mass functions. There are no halos in the lower resolution simulation at $z = 6$, so we start instead at $z = 4$. Most of the differences are in the largest mass bins (at a given redshift) where statistics are poor, and these differences are similar for the simulations with and without corner modes. Thus the presence or absence of corner modes in initial conditions appears to have no effect on the correspondence between halo mass functions of low resolution and high resolution simulations at $z < 4$.

3.4. *Halo Profiles*

As seen in Figure 8, the largest difference in the density 1-point PDF is at high densities, thus we expect the presence or absence of corner modes to have some effect on the inner regions of halos. To test this, we measure stacked profiles of all halos (in different mass bins) at several redshifts. Halo centers are measured in SUBFIND for the FOF parent halos as the position of the most bound particle, i.e., the center of the potential well. The density profiles of each halo are measured using all halo particles and then stacked in logarithmic radial bins. Error bars show the standard deviation of the mean halo profile in each radial bin. Though all halos have at least 20 particles, we stack profiles in two bins of particle number (and therefore total mass): 30 to 100 particles (or 2.11×10^{12} to $7.03 \times 10^{12}\, h^{-1}\, M_\odot$), and greater than 100 particles. The minimum radius of the stacked profile is set to the largest minimum radius of the individual profiles of both simulations.

Figure 12 shows the stacked density profiles of halos with 30 to 100 particles at 4 redshifts from $z = 6.2$ to $z = 3.1$. There is very little difference between stacked profiles from simulations with and without corner modes in the initial conditions. As the redshift decreases, there are more halos and the profiles probe smaller radii. The ratios of the profiles from the simulation without to with corner modes are shown in Figure 13, for the same profiles as in Figure 12. The differences are clearly greater for the inner regions of the profiles, but this is where the profiles are not well resolved, and the differences are within the scatter given by the error bars. Note that at higher redshifts than $z = 6.2$, most of the halos have only 20 particles, and at lower redshifts than $z = 3.1$ the differences are even smaller.

At $z = 6.2$ and $z = 5.3$, there are very few halos with more than 100 particles, so in Figure 14 we show the stacked profiles at $z = 4.2$ and $z = 3.1$, respectively, for halos with greater than 100 particles ($M_{\rm tot} > 7.031 \times 10^{12}\, h^{-1}\, M_\odot$). In the bottom panels we plot the ratio of profiles from the simulation without corner modes to that with corner modes. At both redshifts, the profile from the simulation with corner modes included is enhanced with respect to the profile with no corner modes in the smallest radial bin. This difference appears to be more significant for $z = 4.2$ than for $z = 3.1$, which supports the findings of the previous sections that the effect of including or zeroing the corner modes washes out as redshift decreases; however, there are significant caveats.

One caveat is that for all of these profiles, it is im-

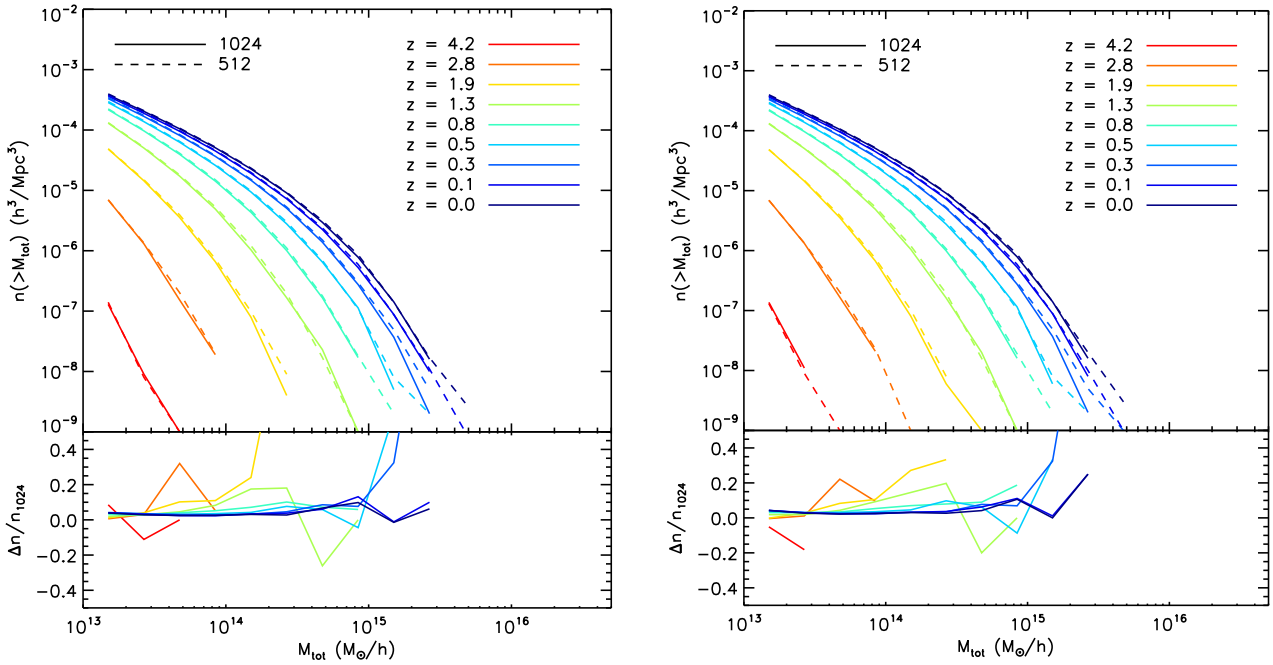

Figure 11. Total mass functions of FOF halos from $z = 4.2$ to $z = 0$ for the zero corner modes simulation (left) and the simulation with corner modes (right) with 1024^3 particles (solid) and at lower resolution with 512^3 particles (dashed). Bottom panels: ratio of mass functions at low resolution to those at high resolution.

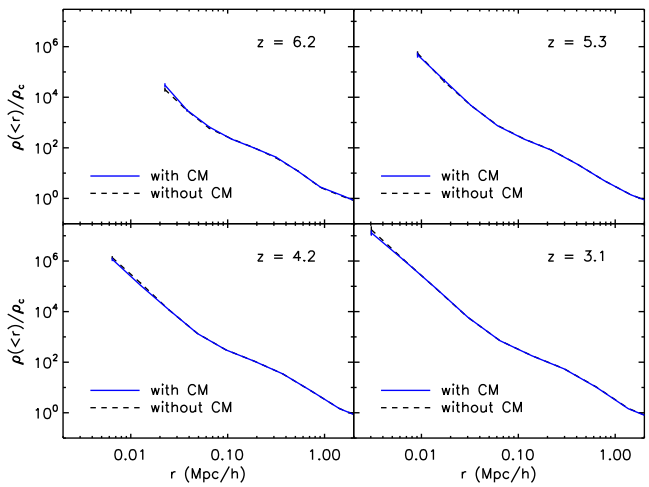

Figure 12. Halo density profiles at $z = 6.2$, 5.3, 4.2, and 3.1 for halos with greater than 30 particles and fewer than 100 particles.

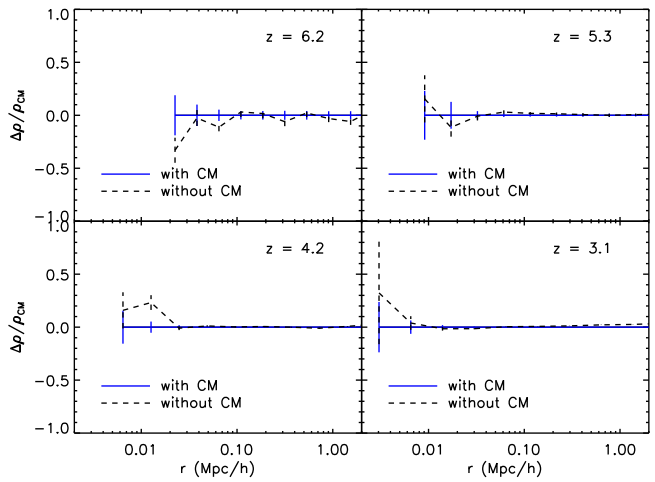

Figure 13. Ratio of stacked halo density profiles of simulation without corner modes to with corner modes, at $z = 6.2$, 5.3, 4.2, and 3.1 for halos with greater than 30 particles and fewer than 100 particles.

portant to note that the inner regions may not be sufficiently resolved to make strong comparisons between the simulations with and without corner modes. For one thing, at higher redshifts, where we expect the differences to be greater, there are no halos in our simulations with a sufficient number of particles to resolve the density profiles to the precision suggested by e.g. Power et al. (2003). Another caveat is that the small scales that exhibit differences due to the presence of corner modes (e.g. Figure 4), probed by the inner regions of the halos, are smaller than the force softening of the simulations, $\epsilon = 0.04\,h^{-1}\,\mathrm{Mpc}$, below which the mass profile may not be converged (Power et al. 2003). However, these convergence studies were performed for individual halos, not for the stacked halo profiles we show in the figures, which can perhaps be trusted more than individual halo profiles.

In any case, we note again that higher resolution simulations will be able to resolve halos at higher redshifts, where the effect of zeroing corner modes is greater, as shown in Section 3.1. Thus it will be important to consider this effect at high redshift in high resolution simulations, for example to study the formation and structure of the inter-galactic medium or to calculate predictions for the SKA. But for simulations at or below a resolution of $L/N = 0.98\,h^{-1}\,\mathrm{Mpc}$, the effect of corner modes on halo profiles can be neglected.

4. CONCLUSION

A common practice in generating initial conditions of cosmological N-body simulations is to set the power

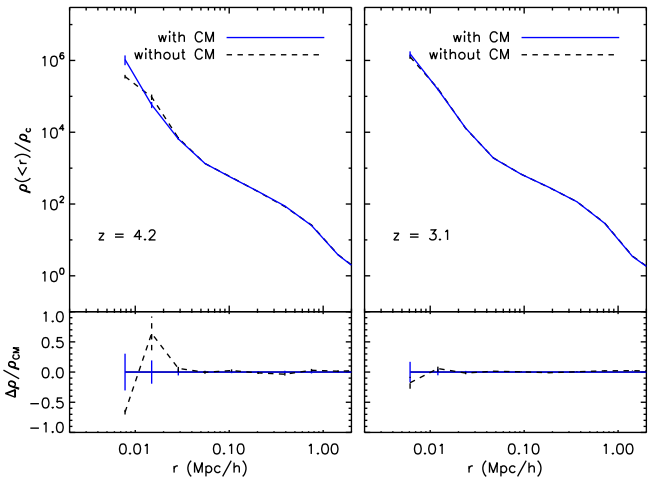

Figure 14. (Top) Stacked halo density profiles and (Bottom) ratio of halo density profiles in the simulation with corner modes to those in the simulation without corner modes, at $z = 4.2$ (left) and $z = 3.1$ (right) for halos with greater than 100 particles.

spectrum to zero at $|\mathbf{k}| > k_{\rm Ny}$, which can be non-zero off the axes of the simulation cube's window function (dubbed 'corner modes'). We have run simulations with and without these corner modes to determine the effect of removing them on statistical measures of large scale structure such as the power spectrum, density 1-point PDF, halo mass function, and halo profiles.

We find that though the difference between the power spectra is largest at high redshift, even at $z = 3$ the difference is at the level of 2% just below $k_{\rm Ny}$ and 0.5% at $k = 2\,h\,{\rm Mpc}^{-1}$ for a simulation with $k_{\rm Ny}$= $3.2\,h\,{\rm Mpc}^{-1}$. Since comparing simulations with and without corner modes doesn't give us an idea of which is 'right,' we also run lower resolution simulations in order to determine whether including or removing these modes results in a better agreement between the low and high resolution simulations. We find that the power spectrum of the lower resolution simulation at its Nyquist frequency is a better match to the higher resolution simulation when the corner modes are present; when zeroed, the ratio of lower to higher resolution $P(k)$ drops sharply at $k_{\rm Ny}$ until $z \sim 6$, while the ratio of simulations with corner modes maintains a smooth transition across the Nyquist boundary. These differences become smaller as $z \to 0$ because the corner modes are repopulated during the evolution of the simulation.

The effect of removing corner modes is greatest at high redshift, high density, and small scales. Zeroing corner modes in initial conditions results in density distribution functions that are narrower with a suppressed high density tail. This difference at high densities is greatest at high redshift, reducing to $\sim 1\%$ at $z = 6$. The variance of the $1\,h^{-1}\,{\rm Mpc}$ CIC overdensity PDF is suppressed by a factor of 2% at $z = 10$ when the corner modes are removed compared to when they are included, reducing to $< 1\%$ at $z = 1$. On the other hand, there is no difference between the variance of $8\,h^{-1}\,{\rm Mpc}$ CIC overdensity PDFs.

Though there are few halos at very high redshift in our simulations, removing corner modes in initial conditions does affect the halo mass function by 3% at $z = 6$ for the smallest halos, with fewer than 50 particles. We found no effect on the correspondence between mass functions in the low and high resolution simulations at $z < 4$, but we note that higher resolution simulations resolve halos at higher redshifts where greater differences were seen in the power spectra and 1-point density PDFs. Similarly, though removing corner modes does affect the inner regions of halo density profiles at high redshift, we did not find these differences to be significant, though we expect the differences to be greater for higher resolution simulations.

Our results suggest that it will be important to include corner modes in simulations that study halos at high redshifts to avoid a suppression of power below the Nyquist frequency and a reduced variance in the 1-point density PDF. We did not find evidence that corner modes introduce unphysical anisotropy into the distribution of dark matter particles, and these modes are repopulated as the simulation evolves even when initially zeroed. Though the effect of corner modes is quite small, at the level of 2% just below $k_{\rm Ny}$ and 0.5% at $k = 2\,h\,{\rm Mpc}^{-1}$ at $z = 3$, sub-percent effects will need to be considered for future surveys such as Euclid, DESI, WFIRST, and SKA.

ACKNOWLEDGEMENTS

The authors are grateful to Adrian Jenkins, Stephane Colombi, and Donghui Jeong for useful discussions and comments on an earlier draft of this manuscript. BF acknowledges financial support from the Research Council of Norway (Programme for Space Research). NM acknowledges support from the European Research Council (DEGAS-259586) and the Science and Technology Facilities Council (ST/L00075X/1). MN was supported at IAP under the ILP LABEX (ANR-10-LABX-63) supported by French state funds managed by the ANR within the Investissements dAvenir programme under reference ANR-11-IDEX-0004-02, and also by ERC Project No. 267117 (DARK) hosted by Universit Pierre et Marie Curie (UPMC) Paris 6, PI J. Silk. JW was supported by NSFC grants 11390372 and 11373029 and the Pilot-B project. MN and AS were supported at JHU by a grant in Data-Intensive Science from the Gordon and Betty Moore and Alfred P. Sloan Foundations.

REFERENCES

Bernardeau, F., Pichon, C., & Codis, S. 2014, Phys. Rev. D, 90, 103519
Bertschinger, E. 1995, ArXiv Astrophysics e-prints, astro-ph/9506070
—. 1998, ARA&A, 36, 599
—. 2001, ApJS, 137, 1
Blas, D., Lesgourgues, J., & Tram, T. 2011, JCAP, 7, 034
Christopherson, A. J., Hidalgo, J. C., Rampf, C., & Malik, K. A. 2015, ArXiv e-prints, arXiv:1511.02220
Codis, S., Pichon, C., Bernardeau, F., Uhlemann, C., & Prunet, S. 2016, MNRAS, 460, 1549
Colombi, S., Jaffe, A., Novikov, D., & Pichon, C. 2009, MNRAS, 393, 511
Crocce, M., Pueblas, S., & Scoccimarro, R. 2006, MNRAS, 373, 369
Davis, M., Efstathiou, G., Frenk, C. S., & White, S. D. M. 1985, ApJ, 292, 371
Efstathiou, G., Davis, M., White, S. D. M., & Frenk, C. S. 1985, ApJS, 57, 241
Eisenstein, D. J., & Hu, W. 1998, ApJ, 496, 605
Garrison, L. H., Eisenstein, D. J., Ferrer, D., Metchnik, M. V., & Pinto, P. A. 2016, ArXiv e-prints, arXiv:1605.02333
Hahn, O., & Abel, T. 2011, MNRAS, 415, 2101
Heitmann, K., White, M., Wagner, C., Habib, S., & Higdon, D. 2010, ApJ, 715, 104

Heitmann, K., Lukić, Z., Fasel, P., et al. 2008, Computational Science and Discovery, 1, 015003
Jenkins, A. 2010, MNRAS, 403, 1859
—. 2013, MNRAS, 434, 2094
Joyce, M., & Marcos, B. 2007, Phys. Rev. D, 75, 063516
Komatsu, E., Smith, K. M., Dunkley, J., et al. 2011, ApJS, 192, 18
Lewis, A., Challinor, A., & Lasenby, A. 2000, ApJ, 538, 473
L'Huillier, B., Park, C., & Kim, J. 2014, New Astronomy, 30, 79
Ma, C.-P., & Bertschinger, E. 1995, ApJ, 455, 7
Marcos, B., Baertschiger, T., Joyce, M., Gabrielli, A., & Sylos Labini, F. 2006, Phys. Rev. D, 73, 103507
McCullagh, N., Jeong, D., & Szalay, A. S. 2016, MNRAS, 455, 2945
Neyrinck, M. C. 2013, MNRAS, 428, 141
Neyrinck, M. C. 2014, in IAU Symposium, Vol. 306, Statistical Challenges in 21st Century Cosmology, ed. A. Heavens, J.-L. Starck, & A. Krone-Martins, 251–254
—. 2016a, MUSCLE: MUltiscale Spherical-ColLapse Evolution, Astrophysics Source Code Library, ascl:1605.007
—. 2016b, MNRAS, 455, L11
Pen, U.-L. 1997, ApJ, 490, L127
Power, C., Navarro, J. F., Jenkins, A., et al. 2003, MNRAS, 338, 14
Reed, D. S., Smith, R. E., Potter, D., et al. 2013, MNRAS, 431, 1866
Salmon, J. 1996, ApJ, 460, 59
Schneider, A., Teyssier, R., Potter, D., et al. 2015, ArXiv e-prints, arXiv:1503.05920
Seljak, U., & Zaldarriaga, M. 1996, ApJ, 469, 437
Sirko, E. 2005, ApJ, 634, 728
Smith, R. E., Reed, D. S., Potter, D., et al. 2014, MNRAS, 440, 249
Springel, V. 2005, MNRAS, 364, 1105
Springel, V., White, S. D. M., Tormen, G., & Kauffmann, G. 2001, MNRAS, 328, 726
Thomas, D. B., Bruni, M., & Wands, D. 2015, MNRAS, 452, 1727
Uhlemann, C., Codis, S., Pichon, C., Bernardeau, F., & Reimberg, P. 2016, MNRAS, 460, 1529
van Daalen, M. P., Schaye, J., Booth, C. M., & Dalla Vecchia, C. 2011, MNRAS, 415, 3649
Zel'dovich, Y. B. 1970, A&A, 5, 84